CLIMATOLOGY

# Rapid Atlantification along the Fram Strait at the beginning of the 20th century

**Tommaso Tesi[1]*†, Francesco Muschitiello[2,3]†, Gesine Mollenhauer[4,5], Stefano Miserocchi[1], Leonardo Langone[1], Chiara Ceccarelli[6], Giuliana Panieri[7], Jacopo Chiggiato[8], Alessio Nogarotto[1,9], Jens Hefter[4], Gianmarco Ingrosso[1], Federico Giglio[1], Patrizia Giordano[1], Lucilla Capotondi[8]**



**The recent expansion of Atlantic waters into the Arctic Ocean represents undisputable evidence of the rapid changes occurring in this region. Understanding the past variability of this "Atlantification" is thus crucial in providing a longer perspective on the modern Arctic changes. Here, we reconstruct the history of Atlantification along the eastern Fram Strait during the past 800 years using precisely dated paleoceanographic records based on organic biomarkers and benthic foraminiferal data. Our results show rapid changes in water mass properties that commenced in the early 20th century—several decades before the documented Atlantification by instrumental records. Comparison with regional records suggests a poleward expansion of subtropical waters since the end of the Little Ice Age in response to a rapid hydrographic reorganization in the North Atlantic. Understanding of this mechanism will require further investigations using climate model simulations.**

## INTRODUCTION

Climate reconstructions of the Common Era are fundamental benchmarks to place human-induced changes into the context of natural climatic change (*1*, *2*). This is particularly relevant for the Arctic, which is currently warming faster than any other region (*3*). Arctic warming has been associated with rapid sea ice decline and expansion of Atlantic waters (AWs) into the Arctic basin (*4*, *5*)—a phenomenon commonly referred to as "Atlantification" (*6*). While in situ observations and satellite images provide high-resolution records of anomalies in water mass properties and sea ice since the 1930s and 1980s (*4*, *7*–*10*), respectively, little is known about this phenomenon in pre- and early-industrial times. Because natural archives preserve evidence of past climate variability, they can offer a longer-term perspective on Atlantification in this region.

The Fram Strait represents an important oceanographic gateway that allows the exchange of Arctic and AW masses (*11*). Low-resolution paleoceanographic records suggest that the summer temperatures of the AW inflow moving along the eastern Fram Strait may have increased before the instrumental record (*12*). Although this change in AW properties hints at a possible early sign of Atlantification, the lack of a reliable chronology for these records limits the integration with regional high-resolution proxy reconstructions to determine the physical mechanisms at play. Recently, it has been argued that the Atlantic subpolar gyre (SPG) has weakened since the 20th century (*13*). This, in turn, might have conditioned the water masses routed toward the Arctic. However, a survey of the recent literature shows that our knowledge primarily hinges on subpolar Atlantic records, while, due to the paucity of Arctic records, polar dynamics still remain elusive (*14*). Therefore, establishing detailed records of Atlantification that stand on robust chronologies is essential to characterize the coupling between midlatitudes and the Arctic region.

In this study, we present a well-dated, subdecadal reconstruction of Atlantification along the eastern Fram Strait using marine sediments from western Svalbard (Kongsfjorden, NYA17-154 core; Fig. 1B). The local oceanographic setting is controlled by the West Spitsbergen Current (WSC), a component of the AW, which supplies heat and salt to the Arctic and is responsible for keeping the eastern Fram Strait ice-free. Our sedimentary record is strategically positioned under the influence of the WSC and polar waters (see spatial correlation analysis at the coring site; fig. S1). Collective evidence from in situ studies indicates a progressive increase of temperature and salinity in Kongsfjorden since instrumental measurements began in the 21st century (*15*–*17*). Thus, our reconstructions here are used to provide a complementary long-term record of the history of Atlantification along the eastern Fram Strait.

Here, we use lipid-based water temperature proxies ($U^{K}_{37}$ and $TEX^{L}_{86}$) and benthic foraminiferal data (distribution and $\delta^{18}O$) to reconstruct changes in water mass properties. Specifically, we examined anomalies in our proxy records to identify diagnostic signs of Atlantification. On the basis of a precise chronology, we combine our results with other local climate records to provide an integrated understanding of Atlantification and resolve its timing. Last, our reconstructions are compared with records of ocean and atmosphere circulation patterns to investigate the connections between the high Arctic and North Atlantic dynamics.

## RESULTS

### Atlantification promotes efficient winter ventilation

The age-depth model of NYA17-154 core (see the "Bayesian age-depth model" section in Methods) indicates relatively high sediment accumulation rates (SARs) over the past 800 years (~0.1 to 0.2 cm/year; fig. S3 and tables S1 and S2). Our records can thus provide evidence at 5- to 10-year resolution of the oceanographic changes that occurred

[1]Istituto di Scienze Polari, Consiglio Nazionale delle Ricerche ISP-CNR, 40129 Bologna, Italy. [2]Department of Geography, University of Cambridge, Cambridge CB2 3EN, UK. [3]NORCE Norwegian Research Centre, 5007 Bergen, Norway. [4]Alfred Wegener Institute, Helmholtz Center for Polar and Marine Sciences, 27570 Bremerhaven, Germany. [5]MARUM Center for Marine Environmental Research, Department of Geosciences, University of Bremen, Bremen, Germany. [6]Dipartimento di Scienze Biologiche, Geologiche ed Ambientali—BiGeA, 40126 Bologna, Italy. [7]CAGE—Center of Arctic Gas Hydrate, Environment and Climate, Department of Geolosciences, UiT The Arctic University of Norway, Tromsø, Norway. [8]Istituto di Scienze Marine–Consiglio Nazionale delle Ricerche ISMAR-CNR, 40129 Bologna, Italy. [9]Campus Scientifico, Università Ca' Foscari Venezia, 30172 Venezia Mestre, Italy.
*Corresponding author. Email: tommaso.tesi@cnr.it
†These authors contributed equally to this work.

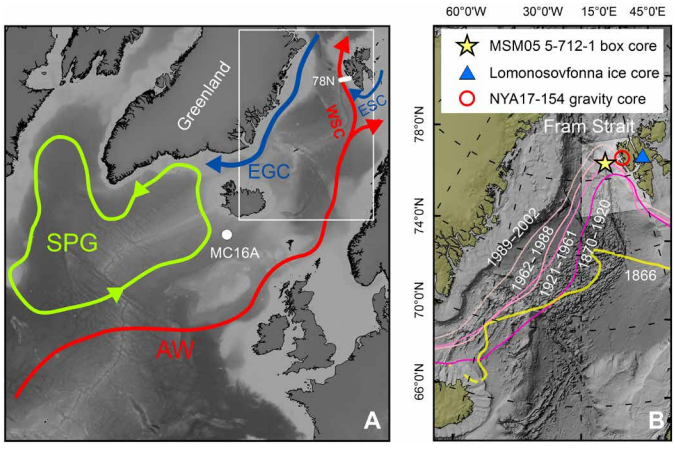


**Fig. 1. Map of the study area.** (**A**) General surface and subsurface circulation in the North Atlantic and Fram Strait. Red and blue dashed lines display waters of Atlantic and Arctic origin, respectively. WSC, West Spitsbergen Current; EGC, East Greenland Current; ESC, East Spitsbergen Current. The green line shows the SPG. The location of the multicore MC16-A is shown as filled white circle (*13*). White line shows the location of the transect across 78°N used to generate time series of hydrographic data displayed in Fig. 4. (**B**) Locations of archive in the Fram Strait. Open red symbol shows the location of core NYA17-154 (this study). Filled blue triangle shows the location of Lomonosovfonna ice core (*19*). Yellow-filled star shows the location of core MSM05/05-712-1 (*12*, *38*). White-shaded area shows the spatial grid considered for the analysis of climate model output presented in Fig. 6 and discussed in the text. Continuous lines display the position of the sea ice edge in April based on data acquired by commercial vessels (*20*) (https://nsidc.org/data/g02169).

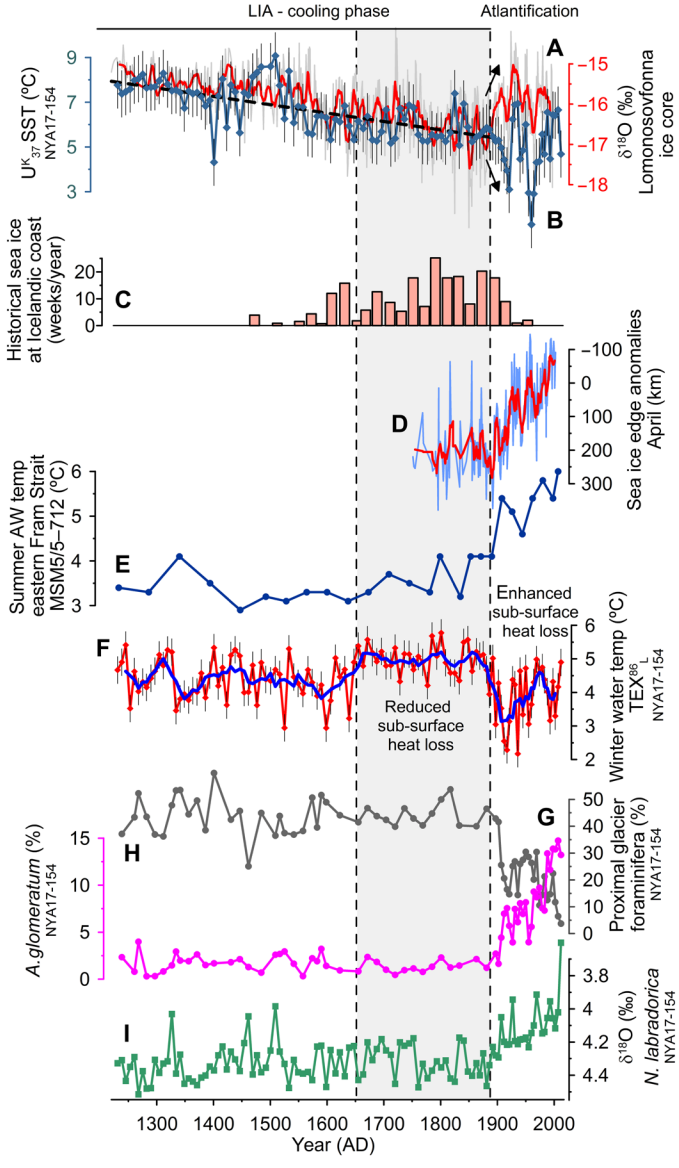


**Fig. 2. Climate variability in the study region.** (**A**) $\delta^{18}O$ of Lomonosovfonna ice core (*19*); red line shows nine-point running average, while the dashed black line shows the linear regression from 1220 to 1890 CE. (**B**) $U^{K}_{37}$-derived SST from core NYA17-154; dashed black line shows the linear fit from 1220 to 1890 CE; the regression line is not visibly distinguishable from the linear fit of Lomonosovfonna ice core data. Standard error is shown as vertical black lines. (**C**) Historical reconstruction of sea ice presence at Icelandic coasts (weeks/year) (*21*). (**D**) April sea ice edge anomalies in the Greenland Sea-Fram Strait (km) (*20*). (**E**) Summer AW temperatures along the eastern Fram Strait MSM5/5-712-1 (°C) based on planktic foraminiferal assemblages (Fig. 1) (*12*). (**F**) $TEX^{86}_{L}$-derived water temperature from core NYA17-154. Standard error is shown as vertical black lines; the gray area displays a period with high values during the LIA. Abundance (%) of *A. glomeratum* (**G**) and proximal glacier foraminifera (*C. reniforme* and *E. excavatum* f. *clavatum*) (**H**) and $\delta^{18}O$ of *N. labradorica* (**I**) from NYA17-154 core.

throughout the coldest phase of the Little Ice Age (LIA) and during the following warm period. Our chronology benefits from a precise stratigraphic constraint offered by a peak in concentration of the retene molecular biomarker, which identifies the beginning of coal mining in 1916 in Kongsfjorden (see Methods and the Supplementary Materials; fig. S3). This age marker provides an accurate time constraint within the 20th century and allows us to precisely calculate the local marine radiocarbon reservoir correction (fig. S3).

$TEX^{L}_{86}$ is a paleo-thermometer of the water column for subpolar/polar regions based on Thaumarchaeota lipids (*18*). Comparison with local reconstructions from the region reveals that the highest $TEX^{L}_{86}$-derived water temperatures occur during the coldest phase of LIA (ca. 1650 to 1900 CE; Fig. 2F, gray area). Specifically, the $\delta^{18}O$ from Lomonosovfonna ice core (Figs. 1B and 2A) (*19*), which primarily reflects large-scale atmospheric temperature, indicates a progressive cooling during the LIA, reaching its peak in the 19th century, before being rapidly interrupted in the 20th century. Similarly, reconstructions based on historical observations indicate protracted presence of sea ice along the Icelandic coasts during the coldest phase of the LIA (Fig. 2C), with an ice edge extending southward well beyond the Fram Strait (e.g., 1866 CE; Fig. 1B) (*20*, *21*).

For the interpretation of $TEX^{L}_{86}$ dataset, the seasonality in production of archaeal lipids and the water depth from which they have originated are two crucial aspects. A recent study (*22*) analyzed the spatiotemporal distribution of Thaumarchaeota along the eastern Fram Strait and found a high abundance of this archaeal group in the epipelagic zone (<200 m) only during dark periods, whereas in the mesopelagic zone (>200 m), Thaumarchaeota were equally abundant in all seasons. Photoinhibition, phytoplanktic competition over ammonia, and nutrient limitations have been suggested by the authors to explain this seasonal pattern (*23*, *24*). Regardless of the driving mechanism, all these scenarios point toward a winter bias for shallow water environments and, considering that Kongsfjorden has a maximum depth of 300 m, we thus interpret our $TEX^{L}_{86}$ dataset primarily as a record of winter temperature of subsurface waters.

Similar winter bias of $TEX_{86}^{L}$ data has been described in the Norwegian Sea (*25*) and in other regions of the Arctic Ocean in modern and paleo studies (*26*, *27*). More generally, this seasonal bias seems to affect shallow water settings (*28*, *29*).

Following this strong evidence from the literature, we infer that the relatively higher $TEX_{86}^{L}$-derived temperature during the coldest phase of LIA is the result of reduced heat loss of subsurface waters because of weak winter mixing, which, in turn, derived from extended sea ice cover that generated a stable and thick halocline (Fig. 3). The opposite phenomenon is well described today in the Artic where sea ice loss is thinning the halocline and promotes winter convection, thus creating favorable conditions for subsurface cooling (*30*). For example, using ocean gliders, a recent study (*31*) showed unprecedented ventilation of AWs in winter due to the retreat of the ice edge. Similar evidence of progressive Atlantification with increased vertical mixing and heat loss in winter was described in the Eurasian Basin and Barents Sea (*4*, *5*); the authors of these studies concluded that, because of the salt and heat redistributions in the upper ocean, winter sea ice formation is further hampered (*5*, *30*, *32*).

This scenario would explain the vigorous winter cooling suggested by $TEX_{86}^{L}$ data associated with the rapid sea ice decline in the 20th century (Figs. 1B, 2C, and 3). It is worth mentioning that, during the same period, reconstructions of summer temperatures indicate an increase of the AW temperature along the eastern Fram Strait (MSM05/05-712-1; Fig. 3E) (*12*). Together, this suggests a multifaceted scenario characterized by a strong seasonality, which highlights the dynamic interactions between sea ice and physical ocean dynamics. This is in line with evidence that ongoing Atlantification is enhancing the seasonal gradient with surface waters becoming more Atlantic from one summer to the next, while in winter convection is progressively more efficient (Fig. 3) (*7*, *31*, *32*).

## Sea ice loss drives timing of primary productivity

In the Arctic, $U_{37}^{K}$ is a proxy for midspring/summer sea surface temperatures (SSTs) based on $C_{37}$-alkenones produced by haptophyte algae *Emiliania huxleyi* and related species (*33*). Overall, SSTs reconstructed with alkenones in our record are higher compared to those obtained with $TEX_{86}^{L}$ (Fig. 2B) despite a couple of intervals in the XX century where the trend is inverted. This further supports the hypothesis that the production of Thaumarchaeota lipids in epipelagic waters mainly occurs in winter.

Unlike $TEX_{86}^{L}$, the $U_{37}^{K}$-derived SSTs exhibit a progressive cooling during the LIA (Fig. 2B). This trend is observed in other proxy-based reconstructions around the Arctic region, including Lomonosovfonna ice core (Fig. 2A), and is reproduced in several simulations (*34*). However, the warming trend that characterized the 20th century in the Arctic (*3*) is not observed in our archive, which, instead, exhibits the lowest SST values.

We argue that this modern cooling reflects the seasonal shift of phytoplankton blooms in response to recent sea ice retreat as suggested by modern evidence in the Arctic where sea ice dynamics control the timing of phytoplankton blooms (*35*, *36*). Historical data from our study region show that, at the onset of the 20th century, the April sea ice edge experienced a rapid retreat (Figs. 1B and 3D) (*20*). Before the 20th century, the eastern Fram Strait was covered by sea ice in April, which likely hampered algal blooms despite the sunlight availability (Fig. 1B). In contrast, the rapid retreat of sea ice in spring since the 20th century likely promoted phytoplankton blooms in ice-free and cold waters like today (Fig. 1B and 3D). Modern primary productivity in the fjord starts in early April (*37*) when surface waters are still cold (ca. 0° to 2°C) compared to the summer temperature (ca. 6° to 8°C, August) (*15*). The strong seasonal gradient illustrates how even a month in advance for phytoplankton to bloom can have a large impact on growth temperatures of phytoplankton and thus on $U_{37}^{K}$-derived SSTs. A previous reconstruction of SSTs based on $U_{37}^{K}$ from the eastern Fram Strait (MSM05/05-712-1; Fig. 1) displayed a cooling trend in recent times, which is coherent with our results (*38*). This cooling has been suggested by the authors to be an expression of the upper mixed layer freshening in response to sea ice loss, which could have released cold and fresh

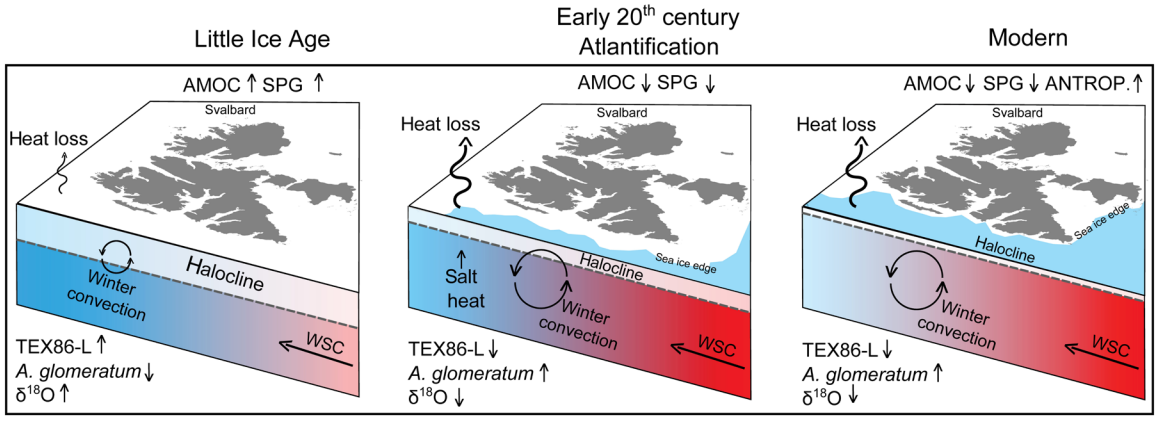


**Fig. 3. Schematic evolution of Atlantification along the Fram Strait during three key periods: Little Ice Age, early 20th century, and modern time.** During the LIA, surface waters along the eastern Fram Strait were characterized by a thick halocline due to the large sea ice extent. In these conditions, heat loss from the surface ocean was reduced because of the stratified water column and the presence of sea ice, which hampered efficient winter convection. With the progressive weakening of the Atlantic meridional overturning circulation (AMOC) at the beginning of the 20th century (Fig. 4), the contraction of the SPG resulted in reduced heat loss from AW waters at subpolar latitudes. The greater heat transport toward the Fram Strait resulted in a rapid sea ice loss and thinning of the halocline. This, in turn, promoted efficient convection with subsequent heat and salt redistribution in subsurface waters that mutually further decreased sea ice formation. During the modern period, anthropogenic-derived forcing (ANTROP) intensified the progressive Atlantification that commenced in the early 20th century. For each period, the schematic figure displays the expected magnitude of the proxies presented in this study.

polar waters into the Fram Strait. However, multiple lines of evidence based on multidecadal in situ measurements (Fram Strait and Barent Sea) and models (*5*, *7*, *9*) indicate that, as the sea ice retreats, the Polar Front moves northward, resulting in a weaker and thinner halocline—a phenomenon that has been ascribed to Atlantification. As a result, surface waters become saltier, less stratified, and eventually more prone to mixing during winter as previously discussed (Fig. 3).

### Response of benthic foraminifera to Atlantification

Recent studies have characterized the modern abundance of live benthic foraminifera in Svalbard fjords under different hydrographic conditions, which ultimately control the habitat of benthic fauna (*39*, *40*). In addition, paleoceanographic studies covering the Holocene provide further details about the response of benthic microfossils to past water mass changes (*41*–*43*).

*Adercotryma glomeratum* is commonly found in Svalbard fjords and belongs to agglutinated species. In Kongsfjorden, *A. glomeratum* exhibits a positive relationship with the bottom water salinity (*39*). Its concentration gradually increases with increasing distance from inner fjord, which highlights its preference for a warm and salty environment bathed by AWs. In our record, *A. glomeratum* shows an abrupt increase in phase with the rapid retreat of sea ice (from ca. 2 to 15%) (Fig. 2G), which indicates a rapid hydrographic change toward an Atlantic domain at the beginning of the 20th century.

*Elphidium excavatum* f. *clavatum* and *Cassidulina reniforme* are two opportunistic proximal-glacier species commonly found close to tidewater glaciers (here combined as "proximal glacier species"; Fig. 2H) (*40*, *44*, *45*). In the modern Kongsfjorden, the two species are relatively abundant in the inner fjord and then markedly decrease with increasing distance from glacier termini (*39*). In our record, these proximal glacier species are the most abundant foraminifera (ca. 50%) throughout the LIA followed by a rapid decrease during the 20th century (ca. 2%) (Fig. 2H and fig. S5). We interpreted this abrupt transition as a rapid retreat of tidewater glaciers in response to AW intrusion (*46*, *47*).

Last, *Nonionellina labradorica* is an Arctic species that commonly flourishes in cold and high productivity conditions (*40*, *43*, *44*). Its presence has been generally associated with the Polar Front position affected by the intrusion of AWs in cold environments. Today, *N. labradorica* is the most common foraminifera in Kongsfjorden, although it does not exhibit a clear relationship with either temperature or salinity (*39*). In our record, the abundance of *N. labradorica* progressively increases during the 20th century until it becomes the dominant species, further supporting the greater influence of AW (fig. S5J). The $\delta^{18}O$ trend of *N. labradorica* mirrors the progressive Atlantification, indicating gradually warmer bottom waters during the 20th century, in particular during recent times (Fig. 2I).

### Link between the high Arctic and North Atlantic circulation

Comparison with in situ measurements acquired since the 20th century along the eastern Fram Strait (*10*) strongly supports the validity of our water property reconstructions. The instrumental data reveal high coherence with our proxies, showing a positive multidecadal temperature trend (transect 61.5°N and 78°N; $P < 0.01$) (Fig. 4). However, these observations cannot resolve the reconstructed regime shift because of the paucity of observations within the first decades of the 20th century and in preindustrial times (Fig. 4A).

To estimate the timing for the onset of Atlantification at our study site, we fitted a multivariate change point model to our paleoceanographic

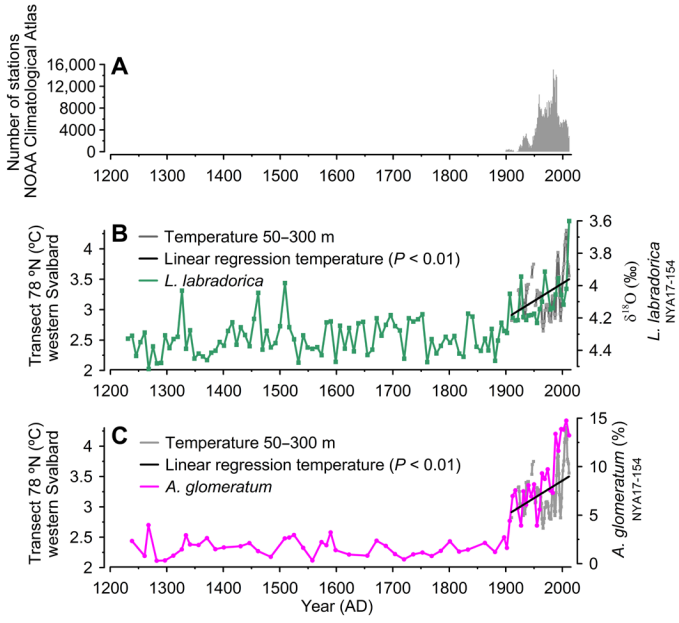


**Fig. 4. Comparison between physical observations along West Spitsbergen and water property proxies from NYA17-154 core.** (**A**) Total number of stations covering the North Atlantic available on NOAA Atlas National Environmental Satellite, Data, and Information Service (*10*). Observations start in the 20th century, although before 1930 measurements were limited and discontinuous. (**B**) Light gray line displays the integrated temperature (50 to 300 m) from transect 78°N in the core of the WSC (Fig. 1). Linear regression ($P < 0.01$) is shown as a black line. Green line displays the $\delta^{18}O$ of *N. labradorica* from core NYA17-154 core. (**C**) Light gray line displays the integrated temperature (50 to 300 m) from transect 78°N in the core of the WSC (Fig. 1) as (B). Linear regression ($P < 0.01$) is shown as a black line. Pink line displays the abundance of *A. glomeratum* from core NYA17-154 core.

records ($TEX_{86}^{L}$ for convection, *A. glomeratum* for salinity, and $\delta^{18}O$ of *N. labradorica* for temperature). This allowed us to detect the common change point structure across independent proxy parameters (see Methods). On the basis of our chronology, the analysis indicates that the timing of the change point occurs within the first two decades of the 20th century (95% credible interval, 1896 to 1917 CE; median, 1907 CE).

To identify the possible mechanisms behind this early onset of Atlantification, we compared our proxy data with records from the subpolar North Atlantic (Fig. 5). Modern studies suggest that the strength of the North SPG regulates the penetration of subtropical waters into the northeast Atlantic (*48*–*51*). On the basis of these observations, it was inferred a weakening of the Atlantic meridional overturning circulation (AMOC) since the end of the LIA coupled with a contraction of the SPG circulation (*13*). We argue that this reduced extension of the SPG likely affected the redistribution of nutrients, heat, and salt in the northeast Atlantic, resulting in an expansion of subtropical waters into the Iceland Basin (*13*) and farther North into the high Arctic.

We test this hypothesis by comparing our records from the Fram Strait with reconstructions of AMOC strength (*52*), and the abundance of *Turborotalita quinqueloba* (%) from the Iceland Basin (Fig. 5, F and G) (*13*). The first parameter is a qualitative indicator of the AMOC derived from SST anomalies in the SPG relative to those in the Northern Hemisphere. Because *T. quinqueloba* prefers cool and productive waters, the latter proxy reflects instead the lateral expansion of

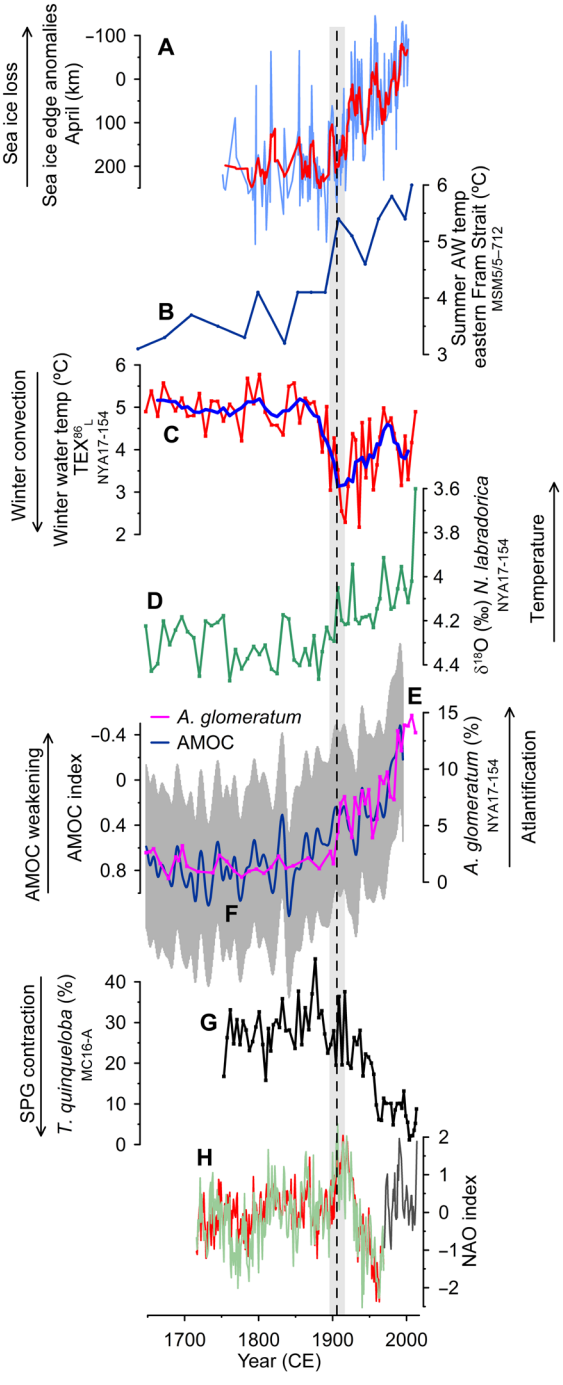


**Fig. 5. Comparison between the Fram Strait and North Atlantic dynamics, 1720 to 2017 CE.** (**A**) April sea ice edge anomalies in the Greenland Sea-Fram Strait (km) (*20*). (**B**) Summer AW temperatures along the eastern Fram Strait MSM5/5-712-1 (°C) based on planktic foraminiferal assemblages. (**C** to **E**) Data from core NYA17-154 (C) $TEX^{86}_{L}$-derived water temperature, (D) $\delta^{18}O$ of *N. labradorica*, and (E) *A. glomeratum* (%). (**F**) AMOC index based on temperature anomalies (*52*). (**G**) *T. quinqueloba* (%) in multicore MC16-A (Fig. 1A) (*13*). (**H**) Red and green lines show the average annual North Atlantic Oscillation (NAO) index based on proxy data/simulations (*62*), whereas the dark gray line displays the modern annual observations (five-point running average) (*63*). Vertical gray bar and black dashed line indicate the 95% credible range (1896 to 1917 CE) and median estimate (1907 CE), respectively, of the timing of the onset of Atlantification in our proxy data derived using a multivariate change point technique (see Methods).

nutrient-poor subtropical waters into the Iceland Basin, which mirrors the contraction of the SPG (*13*). Our comparison reveals high coherence between Arctic and North Atlantic reconstructions, which supports the hypothesis of an SPG control on the northward transport of AW into the high Arctic (*49*, *53*). In particular, the 95% credible intervals obtained from our multiproxy change point model (1896 to 1917 CE) well overlap with independent analyses of change points based on proxies that collectively reflect AMOC and SPG dynamics recently presented (*54*).

Thus, in line with recent findings (*13*), we suggest that the most likely mechanism to explain the early 20th century SPG reconfiguration involves a freshening of the North Atlantic at the end of the LIA and a consequent weakening of the AMOC (*52*, *55*, *56*). This implies a post-LIA scenario characterized by contrasting hydrographic patterns with fresh and cold water spreading into the western SPG, whereas the Svalbard region bathed by the Western Spitsbergen Current experiences a gradual warming and more saline conditions. This interpretation is consistent with a cooling of the subpolar northeast Atlantic and a general weakening of the AMOC evidenced in both modeling studies (*52*, *57*) and reconstructions (Fig. 5) (*54*, *55*, *58*).

Alternatively, the observed changes could be explained by a shift in the dominant mode of the North Atlantic Oscillation (NAO) (*59*). However, despite the fact that the NAO can explain interannual variability of salinity and temperature in the North Sea and Fram Strait driven by wind anomalies (*60*, *61*), its effect on long time scale remains elusive (*51*). We compared our results with the longest reconstruction of NAO index available in literature combined with 20th century measurements (Fig. 5H) (*62*, *63*). The comparison shows that the NAO mode shifted several times over the course of the last centuries but does not exhibit any major regime shift at the time of enhanced Atlantification documented in our reconstruction. Therefore, despite the possible transient effect of NAO on the AW inflow (*64*, *65*), the available reconstructions do not lend support to a driving role for the NAO, whereas our results point toward a possible coupling between the SPG and AMOC systems. We thus suggests that Arctic Atlantification documented in the early 20th century was primarily driven by an oceanographic mechanism—likely a legacy process associated with the end of the LIA— which resulted in a basin-wide reorganization of the North Atlantic Ocean circulation.

Last, we analyzed climate model experiments of the past millennium and historical period to assess the consistency between simulated and observed changes in the rate of Atlantification at the end of the LIA. We investigated simulations from two state-of-the-art Earth System Models that contribute to the Climate Model Intercomparison Project Phase 6 (CMIP6; MIROC-ES2L and MRI-ESM2.0) (*66*). These are currently the only two available CMIP6 historical simulations that have been concatenated to *past1000* simulations (i.e., covering the preindustrial millennium from 850 to 1849 CE) as part of the fourth phase of the Paleoclimate Model Intercomparison Project (PMIP4) (*66*, *67*). For direct comparison with our proxies, we focused on the depth-integrated seasonal salinity and temperature of the upper ocean (250 m) along western Svalbard. The results from the climate simulations are at odds with our reconstructions and show a negligible hydrographic response to post-LIA and historical forcing (Fig. 6). For consistency, we performed a multivariate change point analysis on the output series from the model experiments presented in Fig. 6. However, the analysis failed to identify any notable change point around the onset of the 20th century—a result that is also confirmed by the lack of linear trend changes during the

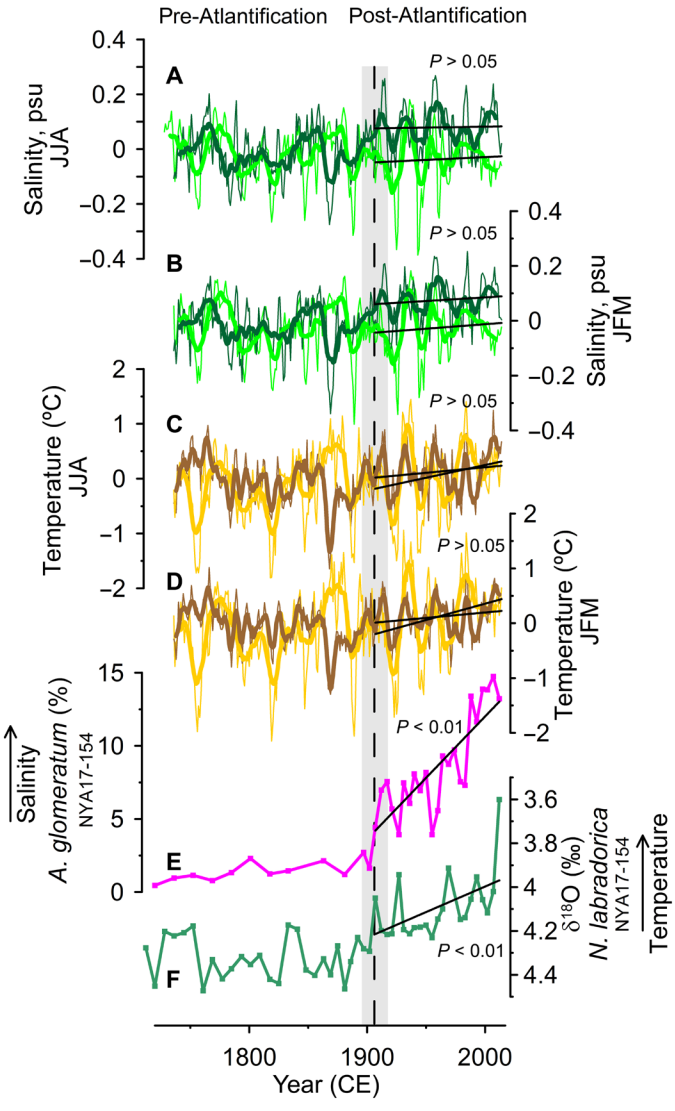


**Fig. 6. Comparison of climate model output and proxies of water mass properties.** (**A** to **D**) Vertically integrated variations in salinity and temperature of the upper ocean (0 to 250 m) along western Svalbard (average across 76°N to 80°N and 0°E to 16°E; Fig. 1B) within PMIP4 last-millennium simulations concatenated to historical simulations from the CMIP6 archive. Dark and light colors display MIROC-ES2L and MRI-ESM2.0 outputs, respectively. JJA refers to June-July-August, whereas JFM refers to January-February-March. Thin and thick lines show the annual and the 5-year running average, respectively. Black lines indicate linear trends fitted to the climate model output (averaged every 5 years) for consistency with our proxy records. (**E**) *A. glomeratum* abundance and (**F**) $\delta^{18}O$ data from core NYA17-154; black lines indicate linear trends fitted to the proxy records. The significance levels of the related slopes based on *P* values are also shown. Trends have been estimated by fitting linear regression models to the data and refer to the period 1907 CE (i.e., onset of Atlantification) to present. Note that the trend is statistically significant ($P < 0.01$) only for *A. glomeratum* (E) and $\delta^{18}O$ (F), whereas the slope of the trends for the climate model output (A to D) is not significant ($P > 0.05$).

past ~100 years (Fig. 6, A to D). We argue that the potential factors responsible for the absence of transient forced behavior in historical runs initialized from the end of the *past1000* simulations can be ascribed to (i) a low sensitivity of North Atlantic circulation and AMOC to early anthropogenic forcing and/or (ii) an underrepresentation in the PMIP4 outcomes of the large-scale legacy resulting from the freshwater input at subpolar latitudes after the LIA—our preferred interpretation.

## DISCUSSION

Our results combined with existing reconstructions demonstrate a rapid and early Atlantification of the eastern Fram Strait at the onset of the 20th century. In particular, we identify the following typical diagnostic signs expressed as anomalies in our proxy records: (i) rapid sea ice edge retreat (ii) and resulting seasonal shift in phytoplankton blooms, (iii) relatively warmer summer waters, (iv) enhanced winter convection in response to a shallower halocline, and (v) marked benthic foraminiferal faunal changes as a result of warmer and saltier water masses. Critically, all the described changes occurred before the ongoing Atlantification documented in the last decade along the route of the Atlantic inflow (*4*, *5*, *7*, *15*).

Our data compared with independent paleoceanographic records suggest that increasing Arctic Atlantification at the start of the industrial era was likely driven by a more efficient poleward heat transport due to a North Atlantic reorganization of the ocean's circulation system. Specifically, the reconstructions point at a weakening of the AMOC and SPG circulation (*13*, *49*, *54*), which resulted in a hydrographic setting that was more conducive to drawing subtropical waters toward the high Arctic (*53*, *68*). We infer that, in line with recent numerical simulations and observational evidence (*49*, *53*, *69*), heat and salt transport toward the Fram Strait likely increased because of reduced surface heat loss and mixing at subpolar latitudes. Moreover, the signs of Atlantification presented here are compatible with self-sustaining mechanism—well documented today (*5*, *30*, *32*)—including salt and heat redistributions in the upper Arctic Ocean due to enhanced convection, which collectively hamper winter sea ice formation (Fig. 3).

Controversy still remains on the relative impact of natural versus anthropogenic forcing on the North Atlantic system. However, it seems likely that the slowdown of the AMOC during the early 20th century has been caused primarily by increased export of Arctic sea ice and freshwater in the North-East Atlantic following the end of the LIA (*52*, *54*–*56*). Farther east, our results from the Fram Strait reveal an opposite scenario characterized by rapid sea ice loss and rapid Atlantification of water masses. Currently, the latest CMIP6 historical climate experiments initialized with transient forcing from PMIP4 last millennium simulations fail to reproduce the post-LIA Atlantification documented in our reconstructions. These findings highlight a potentially important model-data discrepancy that begs for improved historical and preindustrial simulations with better constraints on the freshwater budget of the Arctic and North Atlantic Oceans. Resolving these modeling issues will be crucial to improve the accuracy of projected Atlantification in response to future Arctic warming.

## METHODS

### Sampling and sediment handling

NYA17154 core (112 cm in length) was collected in June 2017 in Kongsfjorden (78°59′52.2' N; 11°39′24″ E; 297 m) using a light gravity corer (weight, 100 kg) on board the *MS Teisten* operated by Kings Bay AS. On the same day of sampling, the core was split in two halves and subsampled with a resolution of 1 cm. Subsamples

were kept frozen until laboratory analyses. Climatological spatial correlations (fig. S1) indicate that the coring site reflects large-scale water mass properties along the eastern Fram Strait.

### Foraminifera assemblages, stable oxygen isotopes ($\delta^{18}O$), and radiocarbon dating

Freeze-dried sediments were washed through a 63-μm sieve and oven-dried at 50°C. Faunally rich samples (fraction >125 μm) were split in aliquots using a dry microsplitter to obtain at least 300 specimens for a valuable representation of microfauna. Species identification was performed as reported in the literature (*39*, *70*). Foraminiferal abundance is expressed as percentage of the total assemblage (%). Calcareous tests of *N. labradorica*, abundant throughout the record, were hand-picked from the dry residue of the >150 μm fraction for isotope measurements ($\delta^{18}O$; between 10 and 15 specimens) and radiocarbon dating (ca. 100 specimens).

$\delta^{18}O$ data (expressed relative to Vienna PeeDee Belemnite) were measured at The Stable Isotope Laboratory at the Arctic University of Norway, UiT. Tests were placed in 4.5-ml vials, flushed with helium, and acidified with five drops of water-free $H_3PO_4$. After equilibration (>2 hours at $T$ = 50°C), samples were analyzed on Gasbench II and MAT253 IRMS (*71*). For each run, instrument uncertainty was <0.1 ‰ based on routine analyses of external standards. Radiocarbon analyses were performed at The Alfred Wegener Institute using a mini radiocarbon dating system (MICADAS) (*72*).

### Lipids

Freeze-dried sediments were transferred into precombusted vials. A known amount of internal standards was added (docosane and $C_{46}$-GDGT) followed by addition of a solvent mixture [dichloromethane: methanol (DCM:MeOH), 9:1, v/v]. Vials were sonicated (15 min at 60°C) and centrifuged, and the supernatant was transferred in precombusted vials. Extraction steps were repeated two more times. Saponification of dry extracts was carried out using 5% methanolic potassium hydroxide at 70°C for 1 hour. The neutral fraction was extracted three times with hexane. Extracts were dried ($N_2$ stream) and redissolved in 500 μl of hexane:DCM (3:2, v/v) before purification via silica gel column chromatography. The apolar fraction was eluted with hexane:DCM (3:2, v/v), and the polar fraction was eluted with MeOH:DCM (1:1, v/v).

In this study, we used the method (*73*) developed for quantifying small amount of alkenones via gas chromatography–mass spectrometry (GC-MS). Briefly, the apolar fraction was redissolved in methyl tert-butyl ether (MTBE:MeOH, 3:1, v/v) with $NaBD_4$ for the conversion of alkenones to alkenols. Excess $NaBD_4$ was neutralized with an aqueous solution of $NH_4Cl$ followed by acidification with HCl and extraction with hexane:DCM (4:1, v/v). Reduced extracts were dried ($N_2$ stream), redissolved in pyridine, and derivatized with bis-trimethylsilyl-trifluoroacetamide for GC-MS analyses.

Retene and alkenones were analyzed using an Agilent 7820A chromatograph fitted with a J&W DB5-MS column (30 m length, 0.25 mm internal diameter, 0.25 mm film thickness) coupled to 5977BMSD. The oven temperature ramp was programmed from 60° to 300°C at 10°C/min (hold time, 10 min). The detector was operated in both selective ion monitoring (SIM) and SCAN modes. Di-, tri-, and tetra-unsaturated $C_{37}$ methyl ketones were quantified integrating the peaks of ion mass/charge ratio ($m/z$) 118 in SIM mode. An example of chromatograms is provided in the Supplementary Materials (fig. S2). Correction factors (conversion of SIM to SCAN areas) were obtained injecting purified amounts of reduced alkenones. Corrected areas were used to calculate the $U^K_{37}$ index as follows (*74*)

$$UK^K_{37} = \left(\frac{C37{:}2\ Me - C37{:}4Me}{C37{:}2\ Me + C37{:}3\ Me + C37{:}4\ Me}\right)$$

SST was estimated using the equation (*75*) used in the Norwegian Sea to reconstruct the SST during Last Termination and Holocene (*76*). Standard error (±1.04°C) has been calculated based on batch culture data and observational data available (*76*). For our record, as observed in the Norwegian Sea (*75*), the SST calculated for the uppermost sediment strata is within the range of the summer temperatures measured in Kongsfjorden (*15*, *16*).

A recent publication has shown the presence of $C_{37}$:4 alkenone-producing isochrysidales associated with sea ice that can affect the overall interpretation of alkenone-derived SST (*77*). As the concentration of $C_{37}$:4 alkenone in our core is relatively low (14.3 ± 2.9%), we believe that our record of $U^K_{37}$ primarily reflects SST dynamics. In addition, it is worth mentioning that (i) the highest $C_{37}$:4 values were measured during the 20th century when it is known that sea ice reached its lowest extent over the studied period and (ii) cultures of isochrysidales show the absence of $C_{38}$ methyl/ethyl alkenones (*77*), whereas our sediments show high abundance of these alkenones that are present instead in *E. huxleyi* (fig. S2).

Retene concentrations were calculated based on the integrated area of TIC or ion $m/z$ 234 depending on the concentration. Integrated peaks of $m/z$ 234 were adjusted for a correction factor based on retene-rich samples to obtain the total ion chromatogram (TIC). Integrated TIC areas were then compared with the response of the internal standard (docosane) to obtain the retene concentration (fig. S3).

The polar GDGT-containing fractions were filtered to remove particles and analyzed using an Agilent 1200 series high-performance liquid chromatography system coupled via an atmospheric pressure chemical ionization interface to an Agilent 6120 MS (APCI-MS) with a method slightly modified from previous reported setting (*78*) to adapt to our equipment. Separation of glycerol dialkyl glycerol tetraethers (GDGTs) (including the 5-/6-methyl isomers of branched-GDGTs) was achieved on two ultraperformance liquid chromatography silica columns in series (Waters Acquity BEH HILIC, 2.1 × 150 mm, 1.7 μm), with a 2.1 × 5 mm precolumn of the same material, maintained at 30°C. Mobile phases A and B consisted of *n*-hexane/chloroform (99:1, v/v) and *n*-hexane/2-propanol/chloroform (89:10:1, v/v/v), respectively. After sample injection (20 μl) and 25-min isocratic elution with 18% mobile phase B, the proportion of B was increased to 50% within 25 min, thereafter to 100% within the next 30 min. After 5 min at 100% B and before the analysis of the next sample, the column was re-equilibrated with 18% B for 15 min. The flow rate was 0.22 ml/min and resulted in a maximum back pressure of 220 bar. The total run time was 100 min.

GDGTs were detected using positive ion APCI-MS and SIM of their $(M+H)^+$ ions (*79*). APCI spray-chamber conditions were as follows: nebulizer pressure, 50 psi; vaporizer temperature, 350°C; N2 drying gas flow, 5 liters/min and 350°C; capillary voltage (ion transfer tube), −4 kV; and corona current, +5 μA. The MS detector was set for SIM of the following $(M+H)^+$ ions: $m/z$ 1302.3 (GDGT-0),

1300.3 (GDGT-1), 1298.3 (GDGT-2), 1296.3 (GDGT-3), 1292.3 (GDGT-4+4′/Crenarchaeol+regio-isomer), 1050 (GDGT-IIIa/IIIa′), 1048 (GDGT-IIIb/IIIb′), 1046 (GDGT-IIIc/IIIc′), 1036 (GDGT-IIa/IIa′), 1034 (GDGT-IIb/IIb′), 1032 (GDGT-IIc/IIc′), 1022 (GDGT-Ia), 1020 (GDGT-Ib), 1018 (GDGT-Ic), and 744 (C46 standard) with a dwell time of 57 ms per ion.

According to the literature (*18*), $TEX_{86}^{L}$ values were calculated as

$$TEX_{86}^{L} = \log\left(\frac{[GDGT-2]}{[GDGT-1]+[GDGT-2]+[GDGT-3]}\right)$$

and converted into temperatures using the following equation developed for the Islandic margin (*26*)

$$SST\,(°C) = 27.898 \times TEX_{86}^{L} + 22.72,;\ n = 21, \pm 0.4°C\ (\text{Standrd Error});\ r2 = 0.73, P < 0.0001) \quad (3)$$

Analytical SD of replicates (external standard) corresponds to ±0.20°C.

## Bayesian age-depth model

For the geochronology, we combined $^{210}$Pb data with five radiocarbon dates measured on tests of *N. labradorica* (fig. S3 and table S1). The activity of the short-lived radionuclide $^{210}$Pb was derived from its daughter nuclide $^{210}$Po via alpha spectrometry. The SAR was estimated using the constant flux–constant sedimentation model (fig. S3) (*80*).

To calibrate radiocarbon dates, we used the Marine13 curve because the recently released Marine20 is not suitable for calibration in polar regions (*81*). The local reservoir effect ($\Delta R$) before calibration was estimated using retene excess as time marker. This organic compound, formed by thermal degradation of higher plant diterpenoids, can trace the release of coal in the fjord from mining activities, which started in Ny-Alesund in 1916 and ended in 1963 (*82*). The base of the retene-rich unit was used to delimit the beginning of the coal extraction in 1916 (fig. S3A). By knowing the year of deposition, the final $\Delta R$ was obtained via radiocarbon dating tests of *N. labradorica* picked from this specific interval. The independent $^{210}$Pb-chronology supports this approach, as the lower limit of the retene-rich unit was dated ca. 1921 CE (95% credible interval, 1912 to 1931; fig. S3 and table S2).

The calculated $\Delta R$ (350 ± 75 years) redefines the reservoir correction for the study region commonly reported in the literature (105 ± 24 years) (*83*) obtained from four dates of mollusks collected around Spitsbergen fjords in 1870 to 1925 CE.

$^{210}$Pb-based SAR profile and $^{14}$C dates were modeled using OxCal4.4 using the P_Sequence deposition procedure and a *k* value (i.e., the parameter that defines the stiffness of the age-depth model upon the dating sequence) of 0.5 cm$^{-1}$ (fig. S4) (*84*). The OxCal age-depth model was run together with the Outlier_Model analysis using the General setting and a prior probability of 0.05, which weighs down the chronological constraints that have a probability >5% of being age reversals. No outliers were detected, and a robust and coherent age model was generated with an agreement index of 225, which is considerably higher than the minimum acceptance threshold of 60.

## Change point analysis

To estimate the timing of the onset of Atlantification in our proxy data, we applied a Bayesian change point analysis method using the "bcp" package in R (*85*). We performed multivariate change point detection to infer the common change point structure across the records that we deemed most sensitive to increased Atlantification (i.e., $TEX_{86}^{L}$, $\delta^{18}O$ of *N. labradorica*, and the abundance of *A. glomeratum*) (Fig. 5). The method assumes that there exists an unknown partition between contiguous blocks of the multivariate dataset such that the mean and variance are constant within each block of each proxy time series but may differ across the time series within a given block. It also assumes that the observations are independent and approximately normally distributed. We tested for a single significant change in the mean values across the three time series and derived the median of the posterior distribution on the location of the change point. To test the sensitivity of the results to the input data, we performed additional univariate analyses on the individual records. The test revealed qualitatively consistent change point estimates and confirmed results from the multivariate analysis.

## Hydrographic data

The in situ temperature dataset is based on the National Oceanic and Atmospheric Administration (NOAA) Climatological Atlas of the Nordic Seas and Northern North Atlantic (*10*). The specific dataset selected is composed of annual gridded yearly fields with $^{1}/_{4}$° horizontal resolution grid of observations collected from 1900 to 2012. Input in situ data have been checked and quality-controlled within the framework of the Global Oceanographic Data Archeology and Rescue Project (*10*). On the basis of the gridded dataset, time series of temperature data are computed. Grid cells of the yearly fields with relative error higher than 0.25 (generally a consequence of a very limited number of input observations) are masked out. To monitor the WSC along western Svalbard (Fig. 1), we generated a time series at polar latitudes (latitude, 78°N; longitude, 8°E to 12°E). The time series of mean temperature profiles was averaged between 50- and 300-m water depth to make it comparable with proxies and filtered with a moving average of 5 years to make the time series consistent to NYA17-154 chronology. Because of the discontinuity of yearly data in the beginning of the time series (mostly before 1950), averages of less than 5 years were retained during the moving averaging process.

## SUPPLEMENTARY MATERIALS

Supplementary material for this article is available at https://science.org/doi/10.1126/sciadv.abj2946

## REFERENCES AND NOTES


1. N. J. Abram, H. V. M. Gregor, J. E. Tierney, M. N. Evans, N. P. Mc Kay, D. S. Kaufman; PAGES 2k Consortium, Early onset of industrial-era warming across the oceans and continents. *Nature* **536**, 411–418 (2016).
2. PAGES2k Consortium, A global multiproxy database for temperature reconstructions of the Common Era. *Sci. Data* **4**, 170088 (2017).
3. N. P. McKay, D. S. Kaufman, An extended Arctic proxy temperature database for the past 2,000 years. *Sci. Data* **1**, 140026 (2014).
4. I. V. Polyakov, A. V. Pnyushkov, M. B. Alkire, I. M. Ashik, T. M. Baumann, E. C. Carmack, I. Goszczko, J. Guthrie, V. V. Ivanov, T. Kanzow, R. Krishfield, R. Kwok, A. Sundfjord, J. Morison, R. Rember, A. Yulin, Greater role for Atlantic inflows on sea-ice loss in the Eurasian Basin of the Arctic Ocean. *Science* **356**, 285–291 (2017).
5. S. Lind, R. B. Ingvaldsen, T. Furevik, Arctic warming hotspot in the northern Barents Sea linked to declining sea-ice import. *Nat. Clim. Chang.* **8**, 634–639 (2018).
6. M. Årthun, T. Eldevik, L. Smedsrud, Ø. Skagseth, R. Ingvaldsen, Quantifying the influence of Atlantic heat on Barents Sea ice variability and retreat. *J. Climate* **25**, 4736–4743 (2012).
7. I. V. Polyakov, M. B. Alkire, B. A. Bluhm, K. A. Brown, E. C. Carmack, M. Chierici, S. L. Danielson, I. Ellingsen, E. A. Ershova, K. Gårdfeldt, R. B. Ingvaldsen, A. V. Pnyushkov,

D. Slagstad, P. Wassmann, Borealization of the Arctic Ocean in response to anomalous advection from sub-Arctic seas. *Front. Mar. Sci.* **7**, 491 (2020).
8. R. Lindsay, A. Schweiger, Arctic sea ice thickness loss determined using subsurface, aircraft, and satellite observations. *Cryosphere* **9**, 269–283 (2015).
9. Q. Wang, C. Wekerle, X. Wang, S. Danilov, N. Koldunov, D. Sein, D. Sidorenko, W.-J. von Appen, T. Jung, Intensification of the Atlantic Water supply to the Arctic Ocean through Fram Strait induced by Arctic sea ice decline. *Geophys. Res. Lett.* **47**, e2019GL086682 (2020).
10. A. Korablev, O. K. Baranova, A. D. Smirnov, D. Seidov, A. R. Parsons, *Climatological Atlas of the Nordic Seas and Northern North Atlantic* (NOAA, 2014).
11. U. Schauer, E. Fahrbach, S. Osterhus, G. Rohardt, Arctic warming through the Fram Strait: Oceanic heat transport from 3 years of measurements. *J. Geophys. Res. Oceans* **109**, C06026 (2004).
12. R. F. Spielhagen, K. Werner, S. A. Sørensen, K. Zamelczyk, E. Kandiano, G. Budeus, K. Husum, T. M. Marchitto, M. Hald, Enhanced modern heat transfer to the Arctic by warm Atlantic water. *Science* **331**, 450–453 (2011).
13. P. T. Spooner, D. J. R. Thornalley, D. W. Oppo, A. D. Fox, S. Radionovskaya, N. L. Rose, R. Mallett, E. Cooper, J. M. Roberts, Exceptional 20th century ocean circulation in the northeast Atlantic. *Geophys. Res. Lett.* **47**, e2020GL087577 (2020).
14. P. Moffa-Sánchez, E. Moreno-Chamarro, D. J. Reynolds, P. Ortega, L. Cunningham, D. Swingedouw, D. E. Amrhein, J. Halfar, L. Jonkers, J. H. Jungclaus, K. Perner, A. Wanamaker, S. Yeager, Variability in the northern North Atlantic and Arctic oceans across the last two millennia: A review. *Paleoceanogr. Paleoclimatol.* **34**, 1399–1436 (2019).
15. A. D'Angelo, F. Giglio, S. Miserocchi, A. Sanchez-Vidal, S. Aliani, T. Tesi, A. Viola, M. Mazzola, L. Langone, Multi-year particle fluxes in Kongsfjorden, Svalbard. *Biogeosciences* **15**, 5343–5363 (2018).
16. H. Hop, F. Cottier, J. Berge, in *The Ecosystem of Kongsfjorden, Svalbard* (Springer, 2019), pp. 515–533.
17. F. Cottier, V. Tverberg, M. Inall, H. Svendsen, F. Nilsen, C. Griffiths, Water mass modification in an Arctic fjord through cross-shelf exchange: The seasonal hydrography of Kongsfjorden, Svalbard. *J. Geophys. Res. Oceans* **110**, C12005 (2005).
18. J.-H. Kim, J. van der Meer, S. Schouten, P. Helmke, V. Willmott, F. Sangiorgi, N. Koç, E. C. Hopmans, J. S. S. Damsté, New indices and calibrations derived from the distribution of crenarchaeal isoprenoid tetraether lipids: Implications for past sea surface temperature reconstructions. *Geochim. Cosmochim. Acta* **74**, 4639–4654 (2010).
19. D. Divine, E. Isaksson, T. Martma, H. A. J. Meijer, J. Moore, V. Pohjola, R. S. W. van de Wal, F. Godtliebsen, Thousand years of winter surface air temperature variations in Svalbard and northern Norway reconstructed from ice-core data. *Polar Res.* **30**, 7379 (2011).
20. D. Divine, C. Dick, Historical variability of sea ice edge position in the Nordic Seas. *J. Geophys. Res. Oceans* **111**, C01001 (2006).
21. H. H. Lamb, *Climatic History and the Future* (*Climate: Present, Past and Future*, vol. 2; Methuen, 1977).
22. O. Müller, B. Wilson, M. L. Paulsen, A. Rumińska, H. R. Armo, G. Bratbak, L. Øvreås, Spatiotemporal dynamics of ammonia-oxidizing thaumarchaeota in distinct arctic water masses. *Front. Microbiol.* **9**, 24 (2018).
23. L. Herfort, S. Schouten, B. Abbas, M. J. W. Veldhuis, M. J. L. Coolen, C. Wuchter, J. P. Boon, G. J. Herndl, J. S. Sinninghe Damsté, Variations in spatial and temporal distribution of Archaea in the North Sea in relation to environmental variables. *FEMS Microbiol. Ecol.* **62**, 242–257 (2007).
24. D. L. Kirchman, H. Elifantz, A. I. Dittel, R. R. Malmstrom, M. T. Cottrell, Standing stocks and activity of Archaea and Bacteria in the western Arctic Ocean. *Limnol. Oceanogr.* **52**, 495–507 (2007).
25. A. Pitcher, C. Wuchter, K. Siedenberg, S. Schouten, J. S. Sinninghe Damsté, Crenarchaeol tracks winter blooms of ammonia-oxidizing Thaumarchaeota in the coastal North Sea. *Limnol. Oceanogr.* **56**, 2308–2318 (2011).
26. D. J. Harning, J. T. Andrews, S. T. Belt, P. Cabedo-Sanz, Á. Geirsdóttir, N. Dildar, G. H. Miller, J. Sepúlveda, Sea ice control on winter subsurface temperatures of the North Iceland shelf during the little ice age: A $TEX_{86}$ calibration case study. *Paleoceanogr. Paleoclimatol.* **34**, 1006–1021 (2019).
27. M. Rodrigo-Gámiz, S. W. Rampen, H. de Haas, M. Baas, S. Schouten, J. S. Sinninghe Damsté, Constraints on the applicability of the organic temperature proxies $U^{K'}_{37}$, $TEX_{86}$ and LDI in the subpolar region around Iceland. *Biogeosciences* **12**, 6573–6590 (2015).
28. A. Leider, K.-U. Hinrichs, G. Mollenhauer, G. J. M. Versteegh, Core-top calibration of the lipid-based U37K and TEX86 temperature proxies on the southern Italian shelf (SW Adriatic Sea, Gulf of Taranto). *Earth Planet. Sci. Lett.* **300**, 112–124 (2010).
29. B. Wei, G. Jia, J. Hefter, M. Kang, E. Park, S. Wang, G. Mollenhauer, Comparison of the $U^{K'}_{37}$, LDI, $TEX^{H}_{86}$, and RI-OH temperature proxies in sediments from the northern shelf of the South China Sea. *Biogeosciences* **17**, 4489–4508 (2020).
30. I. V. Polyakov, A. V. Pnyushkov, E. C. Carmack, Stability of the arctic halocline: A new indicator of arctic climate change. *Environ. Res. Lett.* **13**, 125008 (2018).
31. K. Våge, L. Papritz, L. Håvik, M. A. Spall, G. W. K. Moore, Ocean convection linked to the recent ice edge retreat along east Greenland. *Nat. Commun.* **9**, 1287 (2018).
32. V. Ivanov, A. Smirnov, V. Alexeev, N. V. Koldunov, I. Repina, V. Semenov, Contribution of convection-induced heat flux to winter ice decay in the Western Nansen Basin. *J. Geophys. Res. Oceans* **123**, 6581–6597 (2018).
33. F. G. Prahl, L. A. Muehlhausen, D. L. Zahnle, Further evaluation of long-chain alkenones as indicators of paleoceanographic conditions. *Geochim. Cosmochim. Acta* **52**, 2303–2310 (1988).
34. H. V. McGregor, M. N. Evans, H. Goosse, G. Leduc, B. Martrat, J. A. Addison, P. G. Mortyn, D. W. Oppo, M. S. Seidenkrantz, M. A. Sicre, S. J. Phipps, K. Selvaraj, K. Thirumalai, H. L. Filipsson, V. Ersek, Robust global ocean cooling trend for the pre-industrial Common Era. *Nat. Geosci.* **8**, 671–677 (2015).
35. M. A. Janout, J. Hölemann, A. M. Waite, T. Krumpen, W. J. Appen, F. Martynov, Sea-ice retreat controls timing of summer plankton blooms in the Eastern Arctic Ocean. *Geophys. Res. Lett.* **43**, 12 (2016).
36. L. Oziel, G. Neukermans, M. Ardyna, C. Lancelot, J. L. Tison, P. Wassmann, J. Sirven, D. Ruiz-Pino, J. C. Gascard, Role for Atlantic inflows and sea ice loss on shifting phytoplankton blooms in the Barents Sea. *J. Geophys. Res. Oceans* **122**, 5121–5139 (2017).
37. E. N. Hegseth, P. Assmy, J. M. Wiktor, J. Wiktor Jr., S. Kristiansen, E. Leu, V. Tverberg, T. M. Gabrielsen, R. Skogseth, F. Cottier, Phytoplankton seasonal dynamics in Kongsfjorden, Svalbard and the adjacent shelf, in *The Ecosystem of Kongsfjorden, Svalbard*, H. Hop, C. Wiencke, Eds. (Springer, 2019), pp. 173–227.
38. G. Rueda, S. Fietz, A. Rosell-Melé, Coupling of air and sea surface temperatures in the eastern Fram Strait during the last 2000 years. *Holocene* **23**, 692–698 (2013).
39. P. Jernas, D. Klitgaard-Kristensen, K. Husum, N. Koç, V. Tverberg, P. Loubere, M. Prins, N. Dijkstra, M. Gluchowska, Annual changes in Arctic fjord environment and modern benthic foraminiferal fauna: Evidence from Kongsfjorden, Svalbard. *Glob. Planet. Change* **163**, 119–140 (2018).
40. S. Korsun, M. Hald, Seasonal dynamics of benthic foraminifera in a glacially fed fjord of Svalbard, European arctic. *J. Foraminifer. Res.* **30**, 251–271 (2000).
41. M. Zajączkowski, W. Szczuciński, B. Plessen, P. Jernas, Benthic foraminifera in Hornsund, Svalbard: Implications for paleoenvironmental reconstructions. *Pol. Polar Res.* **31**, 349–375 (2010).
42. T. Rasmussen, M. Forwick, A. Mackensen, Reconstruction of inflow of Atlantic Water to Isfjorden, Svalbard during the Holocene: Correlation to climate and seasonality. *Mar. Micropaleontol.* **94-95**, 80–90 (2012).
43. T. Chauhan, T. L. Rasmussen, R. Noormets, Palaeoceanography of the Barents Sea continental margin, north of Nordaustlandet, Svalbard, during the last 74 ka. *Boreas* **45**, 76–99 (2016).
44. M. Hald, S. Korsun, Distribution of modern benthic foraminifera from fjords of Svalbard, European Arctic. *J. Foraminifer. Res.* **27**, 101–122 (1997).
45. N. Szymańska, J. Pawłowska, M. Kucharska, A. Kujawa, M. Łącka, M. Zajączkowski, Impact of shelf-transformed waters (STW) on foraminiferal assemblages in the outwash and glacial fjords of Adventfjorden and Hornsund, Svalbard. *Oceanologia* **59**, 525–540 (2017).
46. F. A. Holmes, N. Kirchner, J. Kuttenkeuler, J. Krützfeldt, R. Noormets, Relating ocean temperatures to frontal ablation rates at Svalbard tidewater glaciers: Insights from glacier proximal datasets. *Sci. Rep.* **9**, 9442 (2019).
47. A. Luckman, D. I. Benn, F. Cottier, S. Bevan, F. Nilsen, M. Inall, Calving rates at tidewater glaciers vary strongly with ocean temperature. *Nat. Commun.* **6**, 8566 (2015).
48. T. J. Sherwin, J. F. Read, N. P. Holliday, C. Johnson, The impact of changes in North Atlantic Gyre distribution on water mass characteristics in the Rockall Trough. *ICES J. Mar. Sci.* **69**, 751–757 (2012).
49. H. Hátún, A. B. Sandø, H. Drange, B. Hansen, H. Valdimarsson, Influence of the Atlantic subpolar gyre on the thermohaline circulation. *Science* **309**, 1841–1844 (2005).
50. C. Johnson, M. Inall, S. Häkkinen, Declining nutrient concentrations in the northeast Atlantic as a result of a weakening Subpolar Gyre. *Deep–Sea Res. I Oceanogr. Res. Pap.* **82**, 95–107 (2013).
51. V. Koul, C. Schrum, A. Düsterhus, J. Baehr, Atlantic inflow to the North Sea modulated by the subpolar gyre in a historical simulation with MPI-ESM. *J. Geophys. Res. Oceans* **124**, 1807–1826 (2019).
52. S. Rahmstorf, J. E. Box, G. Feulner, M. E. Mann, A. Robinson, S. Rutherford, E. J. Schaffernicht, Exceptional twentieth-century slowdown in Atlantic Ocean overturning circulation. *Nat. Clim. Chang.* **5**, 475–480 (2015).
53. A. Nummelin, C. Li, P. J. Hezel, Connecting ocean heat transport changes from the midlatitudes to the Arctic Ocean. *Geophys. Res. Lett.* **44**, 1899–1908 (2017).
54. L. Caesar, G. D. McCarthy, D. J. R. Thornalley, N. Cahill, S. Rahmstorf, Current Atlantic meridional overturning circulation weakest in last millennium. *Nat. Geosci.* **14**, 118–120 (2021).
55. D. J. R. Thornalley, D. W. Oppo, P. Ortega, J. I. Robson, C. M. Brierley, R. Davis, I. R. Hall, P. Moffa-Sanchez, N. L. Rose, P. T. Spooner, I. Yashayaev, L. D. Keigwin, Anomalously weak Labrador Sea convection and Atlantic overturning during the past 150 years. *Nature* **556**, 227–230 (2018).

56. J. E. Box, W. Colgan, Greenland ice sheet mass balance reconstruction. Part III: Marine ice loss and total mass balance (1840–2010). *J. Climate* **26**, 6990–7002 (2013).
57. L. Caesar, S. Rahmstorf, A. Robinson, G. Feulner, V. Saba, Observed fingerprint of a weakening Atlantic Ocean overturning circulation. *Nature* **556**, 191–196 (2018).
58. B. Thibodeau, C. Not, J. Zhu, A. Schmittner, D. Noone, C. Tabor, J. Zhang, Z. Liu, Last century warming over the Canadian Atlantic shelves linked to weak Atlantic meridional overturning circulation. *Geophys. Res. Lett.* **45**, 12376–12385 (2018).
59. J. W. Hurrell, C. Deser, North Atlantic climate variability: The role of the North Atlantic Oscillation. *J. Mar. Syst.* **78**, 28–41 (2009).
60. M. Bersch, North Atlantic Oscillation–induced changes of the upper layer circulation in the northern North Atlantic Ocean. *J. Geophys. Res. Oceans* **107**, 20-1–20-11 (2002).
61. N. P. Holliday, Air-sea interaction and circulation changes in the northeast Atlantic. *J. Geophys. Res. Oceans* **108**, (2003).
62. P. Ortega, F. Lehner, D. Swingedouw, V. Masson-Delmotte, C. C. Raible, M. Casado, P. Yiou, A model-tested North Atlantic Oscillation reconstruction for the past millennium. *Nature* **523**, 71–74 (2015).
63. J. W. Hurrell, Decadal trends in the North Atlantic Oscillation: Regional temperatures and precipitation. *Science* **269**, 676–679 (1995).
64. T. L. Delworth, F. Zeng, G. A. Vecchi, X. Yang, L. Zhang, R. Zhang, The North Atlantic Oscillation as a driver of rapid climate change in the Northern Hemisphere. *Nat. Geosci.* **9**, 509–512 (2016).
65. M. Muilwijk, L. H. Smedsrud, M. Ilicak, H. Drange, Atlantic Water heat transport variability in the 20th century Arctic Ocean from a global ocean model and observations. *J. Geophys. Res. Oceans* **123**, 8159–8179 (2018).
66. J. H. Jungclaus, E. Bard, M. Baroni, P. Braconnot, J. Cao, L. P. Chini, T. Egorova, M. Evans, J. F. González-Rouco, H. Goosse, G. C. Hurtt, F. Joos, J. O. Kaplan, M. Khodri, K. Klein Goldewijk, N. Krivova, A. N. LeGrande, S. J. Lorenz, J. Luterbacher, W. Man, A. C. Maycock, M. Meinshausen, A. Moberg, R. Muscheler, C. Nehrbass-Ahles, B. I. Otto-Bliesner, S. J. Phipps, J. Pongratz, E. Rozanov, G. A. Schmidt, H. Schmidt, W. Schmutz, A. Schurer, A. I. Shapiro, M. Sigl, J. E. Smerdon, S. K. Solanki, C. Timmreck, M. Toohey, I. G. Usoskin, S. Wagner, C. J. Wu, K. L. Yeo, D. Zanchettin, Q. Zhang, E. Zorita, The PMIP4 contribution to CMIP6 – Part 3: The last millennium, scientific objective, and experimental design for the PMIP4 *past1000* simulations. *Geosci. Model Dev.* **10**, 4005–4033 (2017).
67. M. Kageyama, P. Braconnot, S. P. Harrison, A. M. Haywood, J. H. Jungclaus, B. L. Otto-Bliesner, J. Y. Peterschmitt, A. Abe-Ouchi, S. Albani, P. J. Bartlein, C. Brierley, M. Crucifix, A. Dolan, L. Fernandez-Donado, H. Fischer, P. O. Hopcroft, R. F. Ivanovic, F. Lambert, D. J. Lunt, N. M. Mahowald, W. R. Peltier, S. J. Phipps, D. M. Roche, G. A. Schmidt, L. Tarasov, P. J. Valdes, Q. Zhang, T. Zhou, The PMIP4 contribution to the CIMP6 – Part 1: Overview and over-arching analysis plan. *Geosci. Model Dev.* **11**, 1033–1057 (2018).
68. D. Oldenburg, K. C. Armour, L. Thompson, C. M. Bitz, Distinct mechanisms of ocean heat transport into the Arctic under internal variability and climate change. *Geophys. Res. Lett.* **45**, 7692–7700 (2018).
69. H. Hátún, K. Azetsu-Scott, R. Somavilla, F. Rey, C. Johnson, M. Mathis, U. Mikolajewicz, P. Coupel, J.-É. Tremblay, S. Hartman, S. V. Pacariz, I. Salter, J. Ólafsson, The subpolar gyre regulates silicate concentrations in the North Atlantic. *Sci. Rep.* **7**, 14576 (2017).
70. A. Loeblich, H. Tappan, *Foraminiferal Genera and Their Classification* (Springer, 2015).
71. P.-A. Dessandier, C. Borrelli, H. Yao, S. Sauer, W.-L. Hong, G. Panieri, Foraminiferal $\delta^{18}O$ reveals gas hydrate dissociation in Arctic and North Atlantic ocean sediments. *Geo–Mar. Lett.* **40**, 507–523 (2020).
72. G. Mollenhauer, H. Grotheer, T. Gentz, E. Bonk, J. Hefter, Standard operation procedures and performance of the MICADAS radiocarbon laboratory at Alfred Wegener Institute (AWI), Germany. *Nucl. Instrum. Methods Phys. Res. B* **496**, 45–51 (2021).
73. J.-F. Rontani, S. Wakeham, F. Prahl, F. Vaultier, J. Volkman, Analysis of trace amounts of alkenones in complex environmental samples by way of NaBH4/NaBD4 reduction and silylation. *Org. Geochem.* **42**, 1299–1307 (2011).
74. S. C. Brassell, G. Eglinton, I. T. Marlowe, U. Pflaumann, M. Sarnthein, Molecular stratigraphy: A new tool for climatic assessment. *Nature* **320**, 129–133 (1986).
75. E. Calvo, J. Grimalt, E. Jansen, High resolution U37K sea surface temperature reconstruction in the Norwegian Sea during the Holocene. *Quat. Sci. Rev.* **21**, 1385–1394 (2002).
76. F. G. Prahl, S. G. Wakeham, Calibration of unsaturation patterns in long-chain ketone compositions for palaeotemperature assessment. *Nature* **330**, 367–369 (1987).
77. K. J. Wang, Y. Huang, M. Majaneva, S. T. Belt, S. Liao, J. Novak, T. R. Kartzinel, T. D. Herbert, N. Richter, P. Cabedo-Sanz, Group 2i Isochrysidales produce characteristic alkenones reflecting sea ice distribution. *Nat. Commun.* **12**, 15 (2021).
78. E. C. Hopmans, S. Schouten, J. S. S. Damsté, The effect of improved chromatography on GDGT-based palaeoproxies. *Org. Geochem.* **93**, 1–6 (2016).
79. S. Schouten, A. Forster, F. E. Panoto, J. S. S. Damsté, Towards calibration of the $TEX_{86}$ palaeothermometer for tropical sea surface temperatures in ancient greenhouse worlds. *Org. Geochem.* **38**, 1537–1546 (2007).
80. J. Sanchez-Cabeza, A. Ruiz-Fernández, $^{210}Pb$ sediment radiochronology: An integrated formulation and classification of dating models. *Geochim. Cosmochim. Acta* **82**, 183–200 (2012).
81. T. J. Heaton, P. Köhler, M. Butzin, E. Bard, R. W. Reimer, W. E. N. Austin, C. Bronk Ramsey, P. M. Grootes, K. A. Hughen, B. Kromer, P. J. Reimer, J. Adkins, A. Burke, M. S. Cook, J. Olsen, L. C. Skinner, Marine20—The marine radiocarbon age calibration curve (0–55,000 cal BP). *Radiocarbon* **62**, 779–820 (2020).
82. E. Paglia, A higher level of civilisation? The transformation of Ny-Ålesund from Arctic coalmining settlement in Svalbard to global environmental knowledge center at 79° North. *Polar Rec.* **56**, e15 (2020).
83. J. Mangerud, S. Bondevik, S. Gulliksen, A. K. Hufthammer, T. Høisæter, Marine $^{14}C$ reservoir ages for 19th century whales and molluscs from the North Atlantic. *Quat. Sci. Rev.* **25**, 3228–3245 (2006).
84. C. B. Ramsey, S. Lee, Recent and planned developments of the program OxCal. *Radiocarbon* **55**, 720–730 (2013).
85. C. Erdman, J. W. Emerson, bcp: An R package for performing a Bayesian analysis of change point problems. *J. Stat. Softw.* **23**, 1–13 (2007).
86. S. Levitus, J. I. Antonov, T. P. Boyer, O. K. Baranova, H. E. Garcia, R. A. Locarnini, A. V. Mishonov, J. R. Reagan, D. Seidov, E. S. Yarosh, M. M. Zweng, World ocean heat content and thermosteric sea level change (0–2000 m), 1955–2010. *Geophys. Res. Lett.* **39**, (2012).


**Acknowledgments:** We thank the station *Dirigibile Italia* for providing logistical support at Ny-Ålesund and the captain of *Teisten* for assistance in the field. **Funding:** T.T. acknowledges "Premio Dirigibile Italia" and Fondazione Carisbo (2017/0334) for financial support. This paper is a contribution of the "Centro Aldo Pontremoli" part of the ENI-CNR Joint Research Agreement. The contribution by G.P. is supported by CAGE, through the Research Council of Norway, Centers of Excellence funding scheme grant 287 no. 223259. **Author contributions:** T.T. initiated and led the work. T.T. and S.M. collected the sediment record. G.M. and J.H. analyzed and interpreted the GDGT data. C.C. and A.N. extracted, purified, and analyzed lipids via GC-MS. L.C. analyzed and interpreted the microfaunal data. G.P. analyzed and interpreted the stable oxygen isotopes of foraminifera. F.M. analyzed and interpreted CMIP6 and PMIP4 simulations. L.L. interpreted $^{210}Pb$ dataset. T.T. and F.M. wrote the manuscript. All authors contributed to the final manuscript. **Competing interests:** The authors declare that they have no competing interests. **Data and materials availability:** All data needed to evaluate the conclusions in the paper are present in the paper and/or the Supplementary Materials. Data presented in this study can be found in the open-access repository Zenodo (https://zenodo.org/record/5546419#.YVm-_FXRblU).

Submitted 3 May 2021
Accepted 5 October 2021
Published 24 November 2021
10.1126/sciadv.abj2946

ScienceAdvances

# Rapid Atlantification along the Fram Strait at the beginning of the 20th century

Tommaso TesiFrancesco MuschitielloGesine MollenhauerStefano MiserocchiLeonardo LangoneChiara CeccarelliGiuliana PanieriJacopo ChiggiatoAlessio NogarottoJens HefterGianmarco IngrossoFederico GiglioPatrizia GiordanoLucilla Capotondi

*Sci. Adv.*, 7 (48), eabj2946. • DOI: 10.1126/sciadv.abj2946



*Science Advances* (ISSN ) is published by the American Association for the Advancement of Science. 1200 New York Avenue NW, Washington, DC 20005. The title *Science Advances* is a registered trademark of AAAS.